

Article

Chlorine-Rich $\text{Na}_{6-x}\text{PS}_{5-x}\text{Cl}_{1+x}$: A Promising Sodium Solid Electrolyte for All-Solid-State Sodium Batteries

Yi Zhang ¹, Haoran Zheng ¹, Jiale You ¹, Hongyang Zhao ^{2,*}, Abdul Jabbar Khan ¹, Ling Gao ^{1,*} and Guowei Zhao ^{1,*}

¹ College of Chemistry and Chemical Engineering, Huanggang Normal University, Huanggang 438000, China; legend10086@163.com (Y.Z.)

² School of Chemistry, Xi'an Jiaotong University, Xi'an 710049, China

* Correspondence: zhaohy_001@xjtu.edu.cn (H.Z.); gaoling@hgnu.edu.cn (L.G.); zhaoguowei@hgnu.edu.cn (G.Z.)

Abstract: Developing argyrodite-type, chlorine-rich, sodium-ion, solid-state electrolytes with high conductivity is a long-term challenge that is crucial for the advancement of all-solid-state batteries (ASSBs). In this study, chlorine-rich, argyrodite-type $\text{Na}_{6-x}\text{PS}_{5-x}\text{Cl}_{1+x}$ solid solutions were successfully developed with a solid solution formation range of $0 \leq x \leq 0.5$. $\text{Na}_{5.5}\text{PS}_{4.5}\text{Cl}_{1.5}$ ($x = 0.5$), displaying a highest ionic conductivity of 1.2×10^{-3} S/cm at 25 °C, which is more than a hundred times higher than that of $\text{Na}_6\text{PS}_5\text{Cl}$. Cyclic voltammetry and electrochemical impedance spectroscopy results demonstrated that the rich chlorine significantly enhanced the ionic conductivity and electrochemical stability, in addition to causing a reduction in activation energy. The $\text{Na}_{5.5}\text{PS}_{4.5}\text{Cl}_{1.5}$ composite also showed the characteristics of a pure ionic conductor without electronic conductivity. Finally, the viability of $\text{Na}_{5.5}\text{PS}_{4.5}\text{Cl}_{1.5}$ as a sodium electrolyte for all-solid-state sodium batteries was checked in a lab-scale ASSB, showing stable battery performance. This study not only demonstrates new composites of sodium-ionic, solid-state electrolytes with relatively high conductivity but also provides an anion-modulation strategy to enhance the ionic conductivity of argyrodite-type sodium solid-state ionic conductors.



Citation: Zhang, Y.; Zheng, H.; You, J.; Zhao, H.; Khan, A.J.; Gao, L.; Zhao, G. Chlorine-Rich $\text{Na}_{6-x}\text{PS}_{5-x}\text{Cl}_{1+x}$: A Promising Sodium Solid Electrolyte for All-Solid-State Sodium Batteries. *Materials* **2024**, *17*, 1980. <https://doi.org/10.3390/ma17091980>

Academic Editors: Claudio Gerbaldi, Cataldo Simari, Francesca Soavi, Federico Poli, Akiko Tsurumaki and Alessandro Piovano

Received: 25 March 2024
Revised: 20 April 2024
Accepted: 22 April 2024
Published: 24 April 2024



Copyright: © 2024 by the authors. Licensee MDPI, Basel, Switzerland. This article is an open access article distributed under the terms and conditions of the Creative Commons Attribution (CC BY) license (<https://creativecommons.org/licenses/by/4.0/>).

Keywords: $\text{Na}_6\text{PS}_5\text{Cl}$; sodium solid electrolyte; all-solid-state batteries; ionic conductivity; high electrochemical stability

1. Introduction

Sodium-ion batteries (SIBs) have been considered a highly promising alternative to commercialized lithium-ion batteries (LIBs) due to the natural abundance of sodium resources (2.64 wt% for Na against 0.0017 wt% for Li) and their higher safety levels with similar charge/discharge mechanism [1]. Unfortunately, conventional SIBs face environmental and safety issues originating from the effumability and leakage of flammable organic liquid electrolytes [2,3]. Employing solid-state electrolytes (SSEs) instead of liquid organic electrolytes is a viable solution to the battery issues, since inorganic SSEs are non-volatile and non-flammable [4–6]. Therefore, the rational design of advanced sodium SSEs has been treated as a reliable way to achieve high-performance SIBs.

Sodium-based SSEs have been well developed in recent year and can be roughly divided into oxide-type and sulfide-type SSEs. Oxide-type SSEs such as β -alumina [7,8], NASICON-type $\text{Na}_{1+x}\text{Zr}_2\text{Si}_x\text{P}_{3-x}\text{O}_{12}$ [9,10], and $\text{Na}_2\text{M}_2\text{TeO}_6$ ($M = \text{Zn}$, or Mg) [11–13] exhibit good ionic conductivity of 10^{-4} – 10^{-3} S/cm. However, their poor interfacial compatibilities with electrodes lead to high contact resistances, which hinder the practical fabrication of all-solid-state sodium batteries at room temperature [14]. In contrast, sulfide materials are highly mechanically deformable and have excellent interfacial contact with active materials simply upon cold pressing [15,16]. The development of sodium-based sulfide conductors can be dates to 1992, when a homolog of a thio-LISICON-type, sulfide-based

Na_3PS_4 sodium-ionic conductor with relatively high ionic conductivity was reported not long after the discovery of the well-known Li_3PS_4 lithium-ionic conductor in 1984 [17,18]. Since then, numerous studies have focused on the investigation of sulfide-based SSEs for SIBs [19–21]. Analogous ionic conductors such as Na_3SbS_4 have been synthesized and described in detail [22], while element-doping and defect-introducing strategies have been utilized to promote their electrochemical performance and air stability [2,15,23–28]. Moreover, inspired by the remarkable super-high ionic conductivity of thio-phosphate-type $\text{Li}_{10}\text{GeP}_2\text{S}_{12}$ (LGPS, 12 mS/cm) sulfide electrolytes [29–32], a series of $\text{Na}_{10}\text{MP}_2\text{S}_{12}$ ($M = \text{Ge, Si, Sn}$) sulfide compounds was predicted through first-principles calculations, and new Na-ion conductors, $\text{Na}_{10+x}\text{Sn}_{1+x}\text{P}_{2-x}\text{S}_{12}$ ($x = 0, 1$) with tetragonal phases, have been successfully synthesized, possessing high ionic conductivity at ambient temperature [33–36]. However, Sn^{4+} in the SSE is potentially active when equipped with a highly reductive sodium metal anode, which might result in interfacial instability [37]. Therefore, a highly stable sodium SSE with high ionic conductivity is urgently needed.

Argyrodite-type conductors with high ionic conductivity and stable interfacial properties have been considered as promising electrolytes for all-solid-state batteries due to the absence of transition-metal species [38,39]. The $\text{Li}_6\text{PS}_5\text{X}$ lithium-based conductor ($X = \text{Cl, Br, and I}$) showed their promising properties as an SSE, whereas few reports are available on its sodium analogs. Nevertheless, in previous reports, an argyrodite-type conductor, $\text{Na}_6\text{PS}_5\text{Cl}$, was synthesized [40]. Unexpectedly, the ion conductivity of $\text{Na}_6\text{PS}_5\text{Cl}$ was only 1.2×10^{-5} S/cm, which was significantly lower than that of its $\text{Li}_6\text{PS}_5\text{Cl}$ analog (3×10^{-3} S/cm) [41]. The electrochemical window of $\text{Na}_6\text{PS}_5\text{Cl}$ is only 1.3 V, which makes it impossible for practical use. Increasing the degree of structure disorder by raising the halide content of electrolytes can strengthen the diffusivity of ions in the SSE [41,42]. Therefore, increasing the Cl and Na vacancy contents in $\text{Na}_6\text{PS}_5\text{Cl}$ is favorable for the promotion of $\text{Cl}^-/\text{S}^{2-}$ disordering, as well as Na-ion mobility.

In this work, a highly conductive chlorine-rich sodium solid electrolyte, $\text{Na}_{5.5}\text{PS}_{4.5}\text{Cl}_{1.5}$, was successfully synthesized by increasing Cl and Na vacancy contents with an outstanding conductivity of 1.2×10^{-3} S/cm at room temperature, which is almost ten-fold greater than that of pristine $\text{Na}_6\text{PS}_5\text{Cl}$. The introduction of Cl and Na vacancy contents in $\text{Na}_6\text{PS}_5\text{Cl}$ induced a significant disordering of $\text{S}^{2-}/\text{Cl}^-$ arrangement, leading to the lowering of the activation barriers. Moreover, the electrochemical window of the Cl-rich SSE increased to 2 V, which makes the SSE a practical candidate for ASSBs. We demonstrated the availability of the chlorine-rich $\text{Na}_{5.5}\text{PS}_{4.5}\text{Cl}_{1.5}$ SSE by assembling a $\text{Na}_3\text{V}_2(\text{PO}_4)_3/\text{Na}_{5.5}\text{PS}_{4.5}\text{Cl}_{1.5}/\text{Na}$ full battery, indicating the practical application value of the new $\text{Na}_{5.5}\text{PS}_{4.5}\text{Cl}_{1.5}$ sulfide electrolyte for ASSBs.

2. Materials and Methods

2.1. Materials Synthesis

$\text{Na}_{6-x}\text{PS}_{5-x}\text{Cl}_{1+x}$ ($x = 0, 0.1, 0.2, 0.3, 0.4, 0.5,$ and 0.6) was synthesized by a high-temperature, solid-state reaction method. Stoichiometric Na_2S , P_2S_5 , and NaCl (all chemicals with a purity of 99.99%; Macklin Biochemical Co., Ltd., Shanghai, China) were weighed by chemical stoichiometry in an Ar-filled glovebox (<1 ppm of O_2 , H_2O) and sealed in a 45 mL ZrO_2 pot with 15 ZrO_2 balls with 10 mm diameters and 40 ZrO_2 balls with 5 mm diameters. The raw materials were ball-milled with a planetary ball mill apparatus (YXQM-0.45L, Changsha Mitrcn Instrument Equipment Co., Ltd., Changsha, China) at a rotational speed of 400 rpm for 8 h. Then, the obtained precursors were pelleted at 20–30 MPa in an Ar-filled glovebox (<1 ppm of O_2 , H_2O), sealed in an evacuated Pyrex tube at pressures below 2×10^{-3} Pa, and sintered at 450 °C for 12 h with a heating rate of 2 °C/min. After naturally cooling to room temperature, the as-synthesized $\text{Na}_{6-x}\text{PS}_{5-x}\text{Cl}_{1+x}$ was transferred to a glovebox and mixed by hand with mortar and pestle for 15 min for further characterization and battery assembly.

2.2. Methods

Powder XRD measurements were conducted using a diffractometer equipped with $\text{CuK}\alpha_1$ radiation (XRD-6010, Shimadzu, Tokyo, Japan) to ascertain the phase compositions of the synthesized powders. Prior to XRD measurements, samples were prepared in a glove box and sealed with polyimide film (Dongguan Meixin Co., Ltd., Dongguan, China) to shield them from moisture during the measurements. The diffraction data were collected in the 2θ range of 15° to 50° with step widths of 0.01° . The morphology and elemental mapping analyses for the composite powders were obtained using energy-dispersive X-ray spectroscopy (EDS, Bruker QUANTAX, Berlin, Germany), and the obtained samples were examined using a scanning electron microscope (SEM) (JEOL Ltd., JSM-6390, Tokyo, Japan).

The ionic conductivities of the cylindrical solid electrolyte (SE) pellets were assessed using the AC impedance technique with a cell (stainless steel/SE/stainless steel), employing pressurizable sealing molds and measured between 25 and 85°C . This measurement was repeated two or three times, applying 15 mV in the frequency range of 7 MHz to 1 Hz and utilizing a potentiostat electrochemical interface (Bio-Logic SAS, VSP-300, Claix, France). SE pellets with a diameter of 10 mm were fabricated under a pressure of 303 MPa using a polyaryletherketone mold. Electrochemical window measurements were conducted using sodium/solid electrolyte/sodium cells. Typically, 100 mg of SE was pressed at 150 MPa to form a solid pellet. Na metal foil (purity: 99.9%, thickness: 0.1 mm, diameter: 5 mm; 99.9%, MTI Corporation, Shenzhen, China) was placed on the top side of the electrolyte pellet and further pressed at 150 MPa. The electrochemical stability of $\text{Na}_{6-x}\text{PS}_{5-x}\text{Cl}_{1+x}$ series was determined over a wider potential window, and a cyclic voltammetry (CV) test was conducted at a scan rate of 0.1 mV/s between -2.5 and 2.5 V for comparison of the voltage stability region. The stack pressure applied during the tests was about 5 MPa.

An all-solid-state battery employing the obtained chlorine-rich sodium-ionic conductor with the highest ionic conduction as the electrolyte was assembled under a pressure of 6 MPa within an Ar-filled glovebox to evaluate its charge–discharge performance. The battery assembly method and the utilized cathode materials were akin to those documented in previous reports [43]. The details are as follows: Na metal foil served as the anode, while a composite mixture comprising $\text{Na}_3\text{V}_2(\text{PO}_4)_3$ (NVP) and $\text{Na}_{5.5}\text{PS}_{4.5}\text{Cl}_{1.5}$ (NPSC-6) (NVP:NPSC-6 = 7:3) was employed as the cathode. Prior to use, a sieve with a 10 μm mesh was utilized to eliminate large-particle-size powder in $\text{Na}_{5.5}\text{PS}_{4.5}\text{Cl}_{1.5}$. A pellet with a diameter of 10 mm was produced by cold pressing approximately 100 mg of $\text{Na}_{5.5}\text{PS}_{4.5}\text{Cl}_{1.5}$ powder. Subsequently, Na foil (purity: 99.9%; thickness: 0.1 mm; diameter: 5 mm; 99.9%; MTI Corporation, Shenzhen, China) with a Cu mesh (purity: >99.9%; thickness: 0.045 mm; diameter: 8 mm; pore size: 0.4 mm \times 1.5 mm; MTI Corporation, Hefei, China) was successively pressed onto one side of the pellet. On the opposite side of the pellet, the cathode composite (8 mg) with Al mesh (purity > 99.9%; thickness: 0.055 mm; diameter: 10 mm; pore size; 0.4 mm \times 1.5 mm; MTI Corporation, Hefei, China) and an Al foil current collector (thickness: 0.1115 mm; diameter: 10 mm; purity: >99.9%, MTI Corporation, Hefei, China) were then pressed. Charge–discharge measurements were conducted at 25°C , between 1.4 and 1.8 V, and with a current density of 0.03 mA cm^{-2} (0.05 C) using the LANHE CT2001A charge–discharge system (Wuhan LAND Electronics Co., Wuhan, China). The stack pressure applied during the tests was about 5 MPa.

3. Results and Discussion

3.1. Physical Characterization of $\text{Na}_{6-x}\text{PS}_{5-x}\text{Cl}_{1+x}$

$\text{Na}_{6-x}\text{PS}_{5-x}\text{Cl}_{1+x}$ ($x = 0, 0.1, 0.2, 0.3, 0.4, 0.5,$ or 0.6 , denoted as NPSC-0, NPSC-1, NPSC-2, NPSC-3, NPSC-4, NPSC-5, and NPSC-6, respectively) samples were prepared by a solid-state reaction. The XRD patterns of the NPSC-0 sample were similar to those of the related argyrodite-type $\text{Cu}_6\text{PS}_5\text{Br}$, which displayed a monoclinic phase with a Cc space group [44,45]. A structural model of atomic $\text{Na}_6\text{PS}_5\text{Cl}$ was simulated by replacement of Cu and Br in $\text{Cu}_6\text{PS}_5\text{Br}$ with Na and Cl through structural refinement using Vesta software (version 3) [46], as displayed in the inset of Figure 1a. Two different Na^+ sites were

tetrahedrally coordinated. The Na1 site was surrounded by four S atoms, while the Na2 site was encircled by three S atoms and one Cl atom. The obtained NPSC-0 product was a solid block with chartreuse color (Figure 1b), while the outer and inner layers turned yellow in the NPSC-5 sample (Figure 1c,d). Comparisons of XRD patterns with those of other related compounds (such as tetragonal Na_3PS_4 , cubic Na_3PS_4 , and NaCl) are displayed in Figure S1, proving that no Na_3PS_4 or NaCl impurities were included in the NPSC-0 sample. With the increase in x in $\text{Na}_{6-x}\text{PS}_{5-x}\text{Cl}_{1+x}$, the (400) peak gradually shifted to lower 2θ angles, while the (222) peak migrated to higher 2θ angles, indicating the formation of solid solutions in $\text{Na}_{6-x}\text{PS}_{5-x}\text{Cl}_{1+x}$. Further introduction of additional chlorine into the $\text{Na}_{6-x}\text{PS}_{5-x}\text{Cl}_{1+x}$ structure caused exsolution of NaCl impurity at $x = 0.6$ (Figure S2), resulting a decrease in ionic conductivity. Thus, under the present experimental synthesis conditions, it was shown that $\text{Na}_{5.5}\text{PS}_{4.5}\text{Cl}_{1.5}$ ($x = 0.5$) is the limit of solid solution formation in the $\text{Na}_{6-x}\text{PS}_{5-x}\text{Cl}_{1+x}$ system. In other words, $\text{Na}_{6-x}\text{PS}_{5-x}\text{Cl}_{1+x}$ formed solid solutions in the range of $0 \leq x \leq 0.5$.

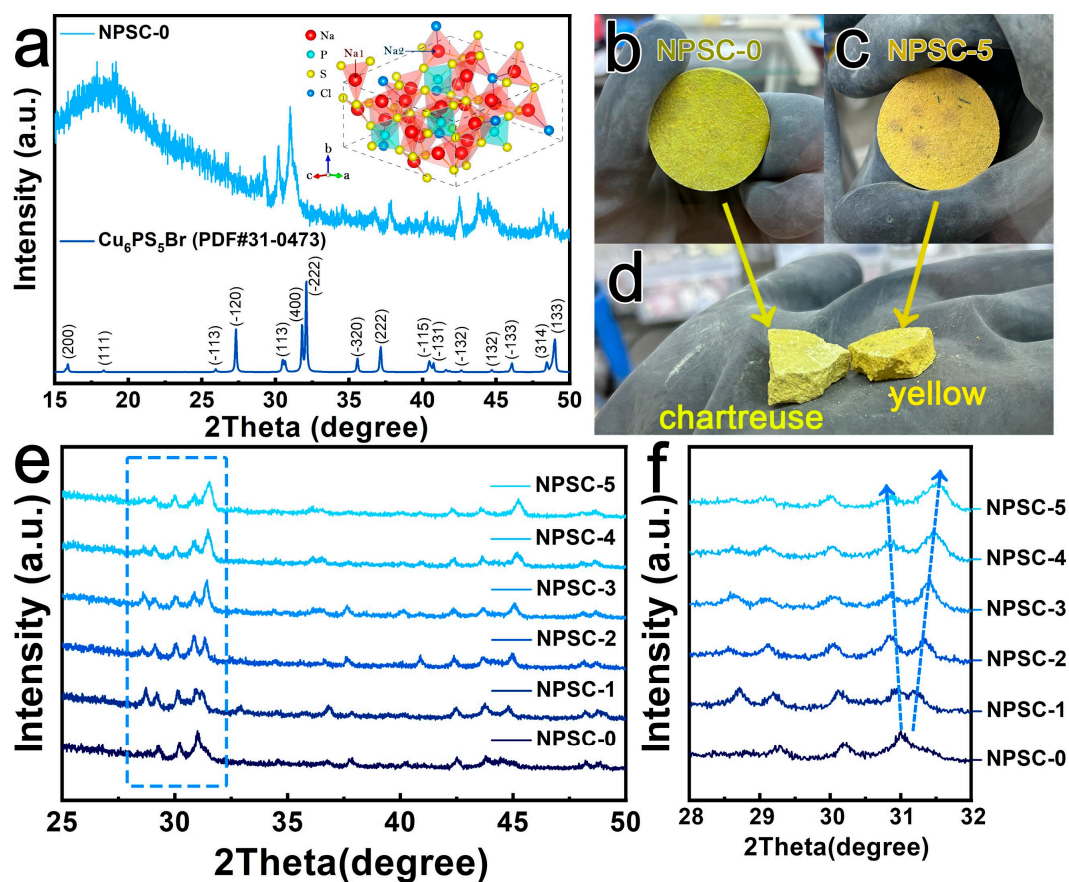


Figure 1. (a) XRD patterns of the $\text{Na}_6\text{PS}_5\text{Cl}$ sample and argyrodite- $\text{Cu}_6\text{PS}_5\text{Br}$ (inset represents the crystal structure model of $\text{Cu}_6\text{PS}_5\text{Br}$). (b,c) Digital images of the synthesized $\text{Na}_{6-x}\text{PS}_{5-x}\text{Cl}_{1+x}$ ($x = 0$ and 0.5) solid block. (d) Comparison of inner color of $\text{Na}_{6-x}\text{PS}_{5-x}\text{Cl}_{1+x}$ ($x = 0$ and 0.6) samples. (e) XRD patterns of $\text{Na}_{6-x}\text{PS}_{5-x}\text{Cl}_{1+x}$ ($x = 0, 0.1, 0.2, 0.3, 0.4$, and 0.5 , denoted as NPSC-0, NPSC-1, NPSC-2, NPSC-3, NPSC-4, and NPSC-5, respectively). (f) Enlarged XRD patterns in the 2θ range of $28\text{--}32^\circ$ from the dotted boxes in (e), the arrows clearly show regular shifting in one direction with increasing Cl content, indicating the formation of solid solutions.

The morphology analysis results showed that the particle sizes of the NPSC-0, NPSC-1, NPSC-2, NPSC-3, NPSC-4 and NPSC-5 samples were in the range of 5 to 50 μm , which was gradually reduced with the increase in the $\text{Cl}^-/\text{S}^{2-}$ ratio, as shown in Figures 2a and S3. The elemental mapping analyses shown in Figure 2b–f indicate the presence and uniform distribution of Na, P, S, and Cl elements within the NPSC-5 sample.

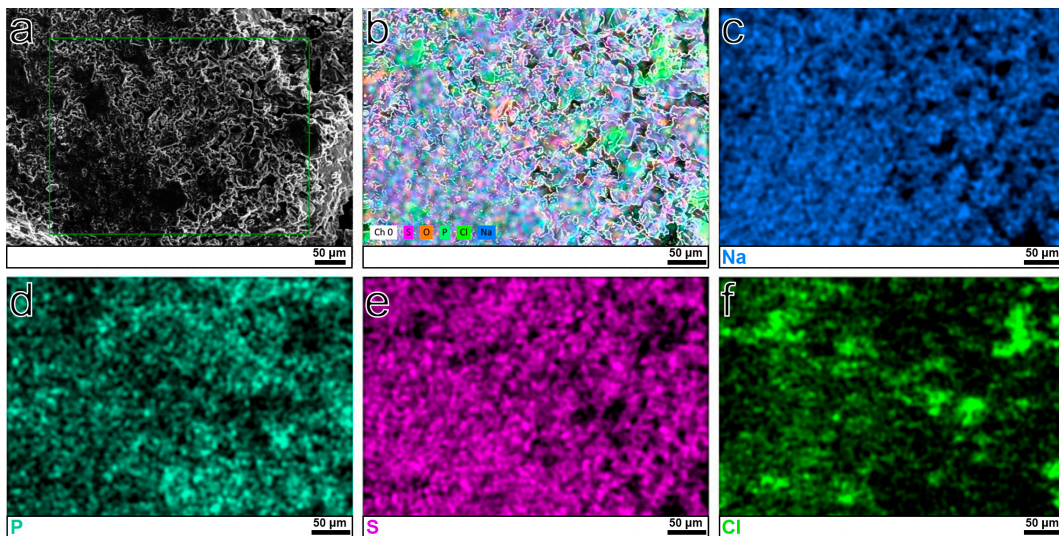


Figure 2. (a) SEM image of NPSC-5 sample. (b–f) EDS element mapping of Na, P, S, and Cl in NPSC-5 sample.

3.2. Electrochemical Performance of $\text{Na}_{6-x}\text{PS}_{5-x}\text{Cl}_{1+x}$ Electrolyte

The electrochemical stability of $\text{Na}_{6-x}\text{PS}_{5-x}\text{Cl}_{1+x}$ was determined for comparison of the voltage stability region, the results of which are shown in Figure 3. The NPSC-0 sample showed a small stable region only at 1.33 V (Figure 3a). With the increase in x in $\text{Na}_{6-x}\text{PS}_{5-x}\text{Cl}_{1+x}$, the voltage stability region widened gradually. When $x = 0.1$, the stable region was at 1.52 V; when $x = 0.2$, the stable region shifted to 1.68 V. It kept increasing to 1.79 and 1.91 V in the NPSC-3 and NPSC-4 samples, respectively. The NPSC-5 sample exhibited a maximum stable voltage of 2.02 V, indicating that promoting the Cl content in $\text{Na}_{6-x}\text{PS}_{5-x}\text{Cl}_{1+x}$ favors the widening of the operating potential window.

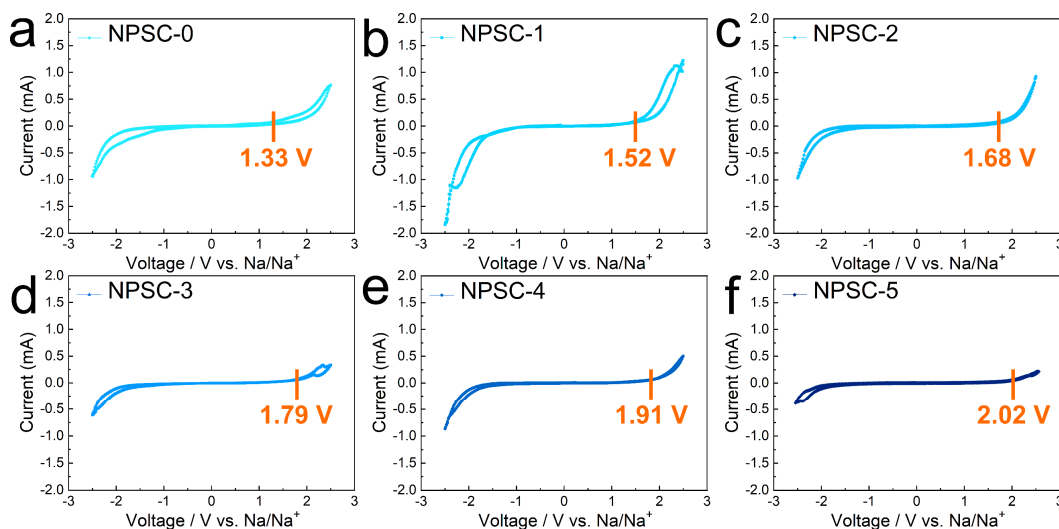


Figure 3. CV curves of (a) Na/NPSC-0/Na, (b) Na/NPSC-1/Na, (c) Na/NPSC-2/Na, (d) Na/NPSC-3/Na, (e) Na/NPSC-4/Na, and (f) Na/NPSC-5/Na with $\text{Na}_{6-x}\text{PS}_{5-x}\text{Cl}_{1+x}$ as analytical materials ($x = 0, 0.1, 0.2, 0.3, 0.4$, and 0.5 , denoted as NPSC-0, NPSC-1, NPSC-2, NPSC-3, NPSC-4, and NPSC-5, respectively) and a scan rate of 0.1 mV/s .

Figure 4 illustrates the complex impedance spectra of the uniaxially cold, isostatic pressed powder samples obtained in the study. The impedance plots exhibit a semicircle pattern accompanied by a spike observed at high and low frequencies, respectively [43]. These features correspond to the total resistance (combining bulk and grain boundary

contributions) and electrode resistances [47]. The semicircle represents ionic transport within the materials, while the spike is indicative of ion-blocking behavior at the interfaces between the electrodes and electrolyte. The equivalent circuits used for impedance analysis, as depicted in Figure S4, were derived from the ZView program [47]. Additionally, the semicircles observed at higher frequencies, displaying capacitances of 10^{-10} F, suggest total resistance, with a combined contribution from both bulk and grain boundaries [48].

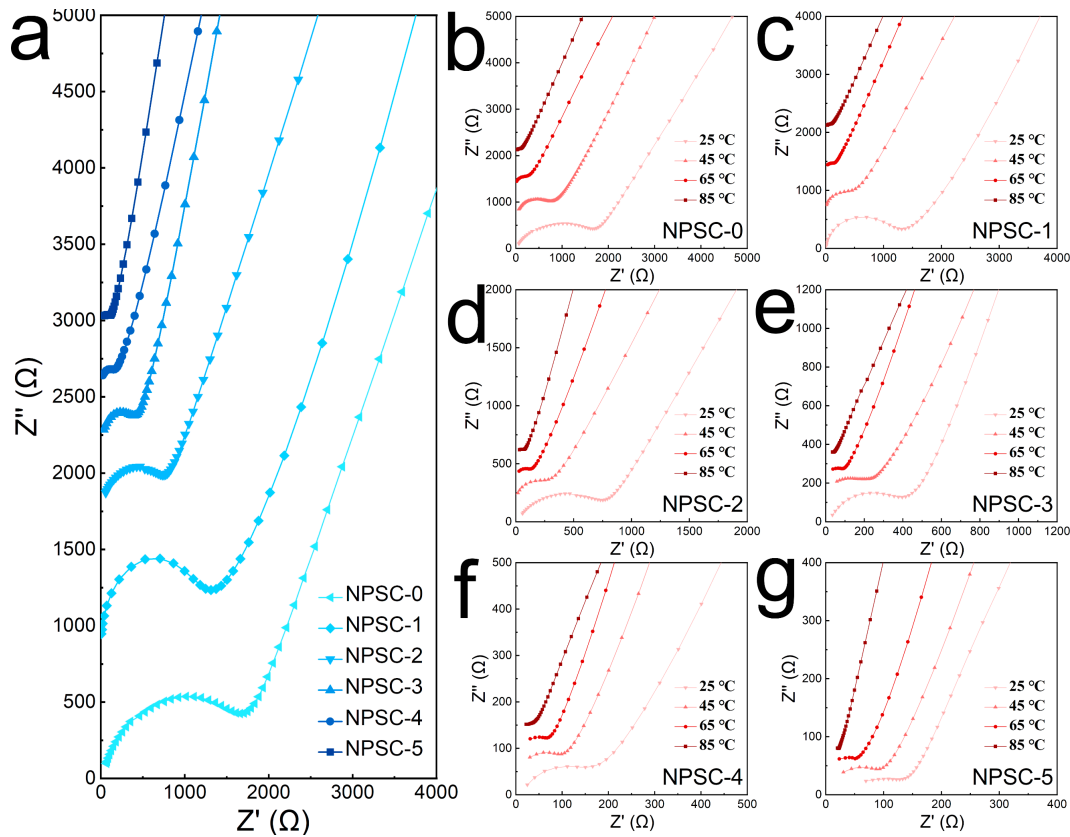


Figure 4. (a) Impedance plots of $\text{Na}_{6-x}\text{PS}_{5-x}\text{Cl}_{1+x}$ samples ($x = 0, 0.1, 0.2, 0.3, 0.4,$ and 0.5 , denoted as NPSC-0, NPSC-1, NPSC-2, NPSC-3, NPSC-4, and NPSC-5, respectively) obtained at 25°C . (b) Impedance plots of the complex impedance responses of (b) NPSC-0, (c) NPSC-1, (d) NPSC-2, (e) NPSC-3, (f) NPSC-4, and (g) NPSC-5 samples measured at $25, 45, 65,$ and 85°C , respectively.

The ionic conductivity of $\text{Na}_{6-x}\text{PS}_{5-x}\text{Cl}_{1+x}$ as analytical material was characterized using the AC impedance method. All the impedance spectra contained formed semicircle pattern at high frequencies attributed to the charge-transfer resistance and an inclined line at low frequencies associated with diffusion processes in the electrodes. With the increase in x in $\text{Na}_{6-x}\text{PS}_{5-x}\text{Cl}_{1+x}$ ($0 \leq x \leq 0.5$), the semicircle diminished gradually, leading to a reduction in resistances by introducing rich Cl contents and facilitating Na^+ diffusion in $\text{Na}_{6-x}\text{PS}_{5-x}\text{Cl}_{1+x}$ (Figure 4a). The calculated ionic conductivities rose gradually with increasing content of Cl, namely 9.4×10^{-5} S/cm for NPSC-0, 1.4×10^{-4} S/cm for NPSC-1, 2.1×10^{-4} S/cm for NPSC-2, 4.2×10^{-4} S/cm for NPSC-3, 7.9×10^{-4} S/cm for NPSC-4, and 1.2×10^{-3} S/cm for NPSC-5. The ionic conductivity of the NPSC-5 sample ($\text{Na}_{5.5}\text{PS}_{4.5}\text{Cl}_{1.5}$ with $x = 0.5$) showed the highest ionic conduction, which was over a hundred times higher than that of $\text{Na}_6\text{PS}_5\text{Cl}$ (1.0×10^{-5} S/cm [40]), proving the importance of increasing the Cl content for Na^+ migration. The NPSC-06 sample displayed a lower ionic conductivity value (2.9×10^{-4} S/cm) than that of NPSC-5 (Figure S4), which could be attributed to the low ionic conductivity of NaCl impurity (Figure S2). The whole testing and disassembly process of the steel/NPSC-5/steel configuration was completed in one shot, which can be observed in Video S1.

All the obtained samples exhibited linear relationships with ionic conductivity in the range of 25–85 °C. Figure 5a illustrates the temperature dependence of ionic conductivity. All obtained samples exhibited linear relationships between ionic conductivity and reciprocal temperature within the studied temperature range, indicating adherence to the Arrhenius law. By applying the Arrhenius equation ($\sigma T = \sigma_0 \exp(-E_a/k_B T)$, where σ_0 references a pre-exponential factor) [49], the activation energy (E_a) of $\text{Na}_{6-x}\text{PS}_{5-x}\text{Cl}_{1+x}$ ($x = 0, 0.1, 0.2, 0.3, 0.4,$ and 0.5) for total conduction was determined from the slope of the plots. In Figure 5b, the composition dependence of the samples' activation energies (E_a) are depicted. AC impedance analysis results revealed that the ionic conductivity of all chlorine-rich $\text{Na}_{6-x}\text{PS}_{5-x}\text{Cl}_{1+x}$ samples was higher than that of the primordial $\text{Na}_6\text{PS}_5\text{Cl}$ ($x = 0$) sample, with ionic conductivity increasing from $x = 0$ to 0.5 . These findings indicate that a rise in chlorine contents can enhance the ionic conductivity of $\text{Na}_6\text{PS}_5\text{Cl}$ with a decrease in E_a . Table S1 summarizes the ionic conductivities and E_a values reported in the literature, as well as the values obtained in this study. Compared with the reported $\text{Na}_6\text{PS}_5\text{Cl}$ (0.01×10^{-3} S/cm) [40], the modified $\text{Na}_{5.5}\text{PS}_{4.5}\text{Cl}_{1.5}$ exhibited superior ionic conductivity of 1.2×10^{-3} S/cm, which is the same order of magnitude as the $\text{Na}_{11}\text{Sn}_2\text{PS}_{12}$ sulfide electrolyte (4×10^{-3} S/cm) reported in [35] and the vacancy-contained Na_3SbS_4 (3×10^{-3} S/cm) reported in [22]. Therefore, $\text{Na}_{5.5}\text{PS}_{4.5}\text{Cl}_{1.5}$ ($x = 0.5$, NPSC-5) shows very high values of ionic conductivity among the typical sodium ion conductors that have been reported.

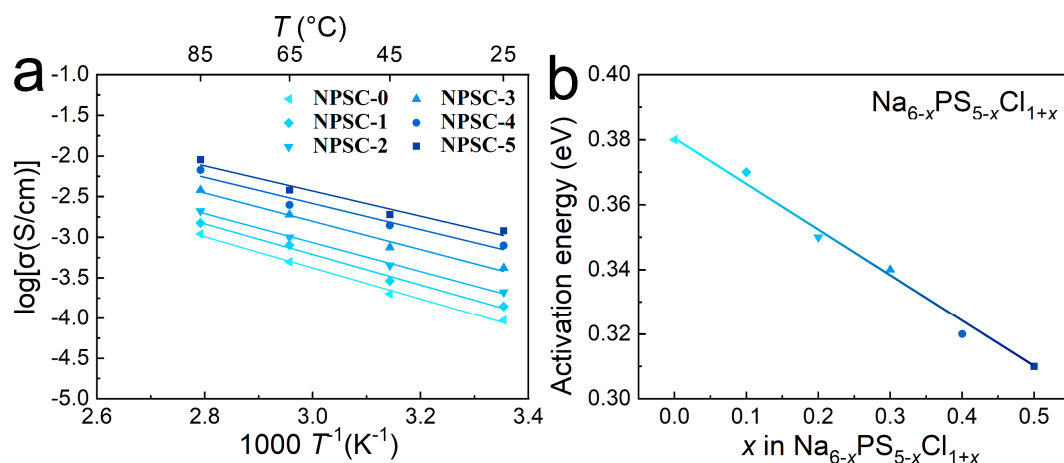


Figure 5. (a) Temperature dependence of the ionic conductivity of XRD patterns of $\text{Na}_{6-x}\text{PS}_{5-x}\text{Cl}_{1+x}$ ($x = 0, 0.1, 0.2, 0.3, 0.4,$ and 0.5 , denoted as NPSC-0, NPSC-1, NPSC-2, NPSC-3, NPSC-4, and NPSC-5, respectively) samples. (b) Activation energies of $\text{Na}_{6-x}\text{PS}_{5-x}\text{Cl}_{1+x}$ at different x values.

3.3. Electrochemical Performance of NVP//NPSC-5//Na ASSB

$\text{Na}_{5.5}\text{PS}_{4.5}\text{Cl}_{1.5}$ ($x = 0.5$, NPSC-5) showed the highest ionic conductivity and lowest activation energy in the $\text{Na}_{6-x}\text{PS}_{5-x}\text{Cl}_{1+x}$ system, so the electrochemical performance of a laboratory-grade, pressurized NVP//NPSC-5//Na cell with NPSC-5 as a sodium solid electrolyte and commercial $\text{Na}_3\text{V}_2(\text{PO}_4)_3$ (NVP, 99.9%, MTI Corporation, Shenzhen, China) and Na metal foil as cathode and anode, respectively, was determined, as depicted in the schematic diagram in Figure 5a. Since NVP can offer a 1.6 V voltage plateau through the $\text{V}^{3+}/\text{V}^{2+}$ redox reaction, which lies within the voltage stability region of the NPSC-5 electrolyte, the galvanostatic charge–discharge of the NVP//NPSC-5//Na ASSB was tested in the potential range of 1.4–1.8 V at a current density of 0.05 C. All charge–discharge profiles exhibited a 1.6 V plateau, corresponding to the phase transition of $\text{Na}_3\text{V}_2(\text{PO}_4)_3/\text{Na}_4\text{V}_2(\text{PO}_4)_3$ with one Na^+ intercalation/deintercalation from the host lattices [50]. The right figure in Figure 6a shows a physical electronic photograph of an assembled all-solid-state sodium-ion battery that can normally light up an LED light bulb at room temperature, indicating that NPSC-5 is a pure sodium-ion conductor material

with negligible electronic conductivity and functions as a solid electrolyte. The additional plateau at about 1.42 V shown in Figure 6b can be attributed to the formation of a stable NPSC-5/Na interface during the first cycle, which was similar to reports of other electrochemical investigations sodium ASSBs [2,51–53]. The NPSC-5/Na interface resulted in a low coulombic efficiency (58%) during the first cycle (The initial discharge capacity was about 81.9 mAh/g, whereas the charge capacity was only 47.3 mAh/g). The second charge and discharge capacities were 43.1 mAh/g and 42.2 mAh/g, respectively, indicating the rebound of coulombic efficiency (98%). The 10th cycle displayed charge and discharge capacities of 34.3 and 33.7 mAh/g, respectively; nearly 73% of the initial charge capacity was retained, and the coulombic efficiency was maintained at 98%, demonstrating that the synthesized material facilitated the cyclic charging and discharging capabilities of the battery. The energy density of the full cell was about 70 Wh/Kg based on the mass of the active cathode. Further modifications, such as to the tips for battery assembly, compositing the NVP cathode with graphene, or replacing the Na disc with a Na-Sn alloy to improve the performance of the NVP//NPSC-5//Na ASSB, should be analyzed and explored in depth in the future.

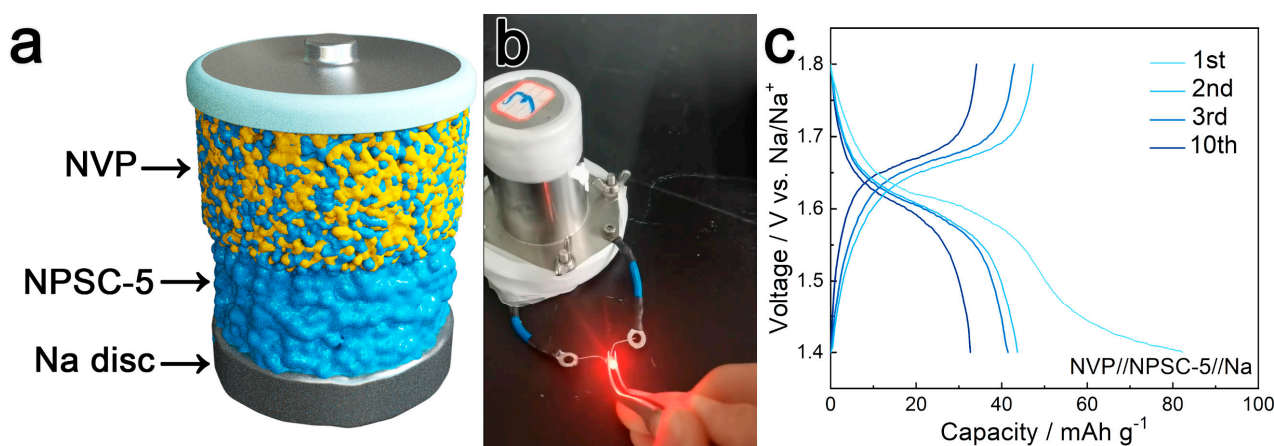


Figure 6. (a) Illustration of a $\text{Na}_3\text{V}_2(\text{PO}_4)_3//\text{NPSC-5//Na}$ ASSB. (b) A digital picture of a $\text{Na}_3\text{V}_2(\text{PO}_4)_3//\text{NPSC-5//Na}$ ASSB working at room temperature to make an LED diode bead light up. (c) Galvanostatic charge–discharge curves of a $\text{Na}_3\text{V}_2(\text{PO}_4)_3//\text{NPSC-5//Na}$ ASSB at 25 °C with a charge–discharge speed of 0.05 C (1 C = 60 mA/g).

4. Conclusions

In summary, halide-rich solid solutions of argyrodite-type $\text{Na}_{6-x}\text{PS}_{5-x}\text{Cl}_{1+x}$ were synthesized and formed solid solutions in the range of $0 \leq x \leq 0.5$. Increasing Cl^- contents effectively reduced the activation barrier and increased the Na-ion mobility, as well as electrochemical stability. The optimal solid solution composition of $\text{Na}_{5.5}\text{PS}_{4.5}\text{Cl}_{1.5}$ exhibited particularly high Na-ion conductivity in the $\text{Na}_{6-x}\text{PS}_{5-x}\text{Cl}_{1+x}$ in this work, namely 1.2 mS/cm at 25 °C, which is more than a hundred times higher than that of $\text{Na}_6\text{PS}_5\text{Cl}$ with a regular composition. Meanwhile, $\text{Na}_{5.5}\text{PS}_{4.5}\text{Cl}_{1.5}$ is more suitable for high-voltage cathodes than $\text{Na}_6\text{PS}_5\text{Cl}$ due to its wider voltage stability region up to 2 V, and the smooth charge–discharge cycling performance of $\text{Na}_3\text{V}_2(\text{PO}_4)_3//\text{Na}_{5.5}\text{PS}_{4.5}\text{Cl}_{1.5}//\text{Na}$ at room temperature verifies that the obtained material is a pure sodium-ion conductor and its potential as a sodium-ionic solid electrolyte for all-solid-state sodium batteries. To date, the reported sulfide electrolyte, $\text{Na}_{11}\text{Sn}_2\text{PS}_{12}$ (4×10^{-3} S/cm) [35] and vacancy-contained Na_3SbS_4 (3×10^{-3} S/cm) [22] have exhibited excellent conductivity. Both references proposed the strategy of designing Na vacancy for the improvement of conductivity. Therefore, we suppose that the ionic conductivity of $\text{Na}_{5.5}\text{PS}_{4.5}\text{Cl}_{1.5}$ could be further promoted by designing Na vacancy in the crystal structure.

Supplementary Materials: The following supporting information can be downloaded at: <https://www.mdpi.com/article/10.3390/ma17091980/s1>, Figure S1: Comparison of XRD patterns for $\text{Na}_6\text{PS}_5\text{Cl}$, cubic $\text{Ag}_{15}\text{P}_4\text{S}_{16}\text{Cl}$, tetragonal Na_3PS_4 , cubic Na_3PS_4 , and NaCl ; Figure S2: XRD patterns of NPSC-5 and NPSC-6 samples and standard- NaCl ; Figure S3: SEM images of (a) NPSC-0, (b) NPSC-1, (c) NPSC-2, (d) NPSC-3, and (e) NPSC-4 samples; Figure S4: The equivalent circuit used to extract the value of resistance from EIS spectra with two semicircles. All EIS spectra of $\text{Na}_{6-x}\text{PS}_{5-x}\text{Cl}_{1+x}$, in general, exhibit two semicircular patterns. The conductivity was computed from the resistance using the following formula: $\text{Conductivity} = \text{Thickness}/(\text{Area} \times \text{Resistance})$; Figure S5: Impedance plot of NPSC-6 sample at 25 °C; Table S1: Comparison of ionic conductivity and activation energy (E_a) obtained in this study with those previously reported; Video S1: Impedance test of NPSC-5 sample.

Author Contributions: Conceptualization, G.Z.; Data curation, Y.Z., H.Z. (Haoran Zheng), J.Y., A.J.K., L.G. and G.Z.; Funding acquisition, Y.Z., L.G. and G.Z.; Investigation, Y.Z., L.G. and G.Z.; Methodology, G.Z.; Project administration, G.Z.; Validation, Y.Z., H.Z. (Hongyang Zhao), L.G. and G.Z.; Visualization, Y.Z., H.Z. (Haoran Zheng), J.Y., H.Z. (Hongyang Zhao), A.J.K. and G.Z.; Writing—original draft, Y.Z. and G.Z.; Writing—review and editing, H.Z. (Hongyang Zhao) and G.Z. All authors have read and agreed to the published version of the manuscript.

Funding: The work performed at Huanggang Normal University was supported by financial support from the National Natural Science Foundation of China (22109049); the Provincial Natural Science Foundation for Distinguished Young Scholars of Hubei Province, China (2023AFA064); the Key Project of Scientific Research Program of Hubei Provincial Department of Education, China (D20222901); and the Key Laboratory of Catalysis and Energy Materials Chemistry of the Ministry of Education and Hubei Key Laboratory of Catalysis and Materials Science (202306).

Institutional Review Board Statement: Not applicable.

Informed Consent Statement: Not applicable.

Data Availability Statement: Data are contained within the article.

Conflicts of Interest: The authors declare no conflicts of interest.

References

1. Vaalma, C.; Buchholz, D.; Weil, M.; Passerini, S. A Cost and Resource Analysis of Sodium-Ion Batteries. *Nat. Rev. Mater.* **2018**, *3*, 18013. [[CrossRef](#)]
2. Moon, C.K.; Lee, H.-J.; Park, K.H.; Kwak, H.; Heo, J.W.; Choi, K.; Yang, H.; Kim, M.-S.; Hong, S.-T.; Lee, J.H.; et al. Vacancy-Driven Na^+ Superionic Conduction in New Ca-Doped Na_3PS_4 for All-Solid-State Na-Ion Batteries. *ACS Energy Lett.* **2018**, *3*, 2504–2512. [[CrossRef](#)]
3. Zhang, Y.; Zhang, R.; Huang, Y. Air-Stable Na_xTMO_2 Cathodes for Sodium Storage. *Front. Chem.* **2019**, *7*, 335. [[CrossRef](#)] [[PubMed](#)]
4. Lu, Y.; Li, L.; Zhang, Q.; Niu, Z.Q.; Chen, J. Electrolyte and Interface Engineering for Solid-State Sodium Batteries. *Joule* **2018**, *2*, 1747–1770. [[CrossRef](#)]
5. Wang, J.; Okabe, J.; Komine, Y.; Notohara, H.; Urita, K.; Moriguchi, I.; Wei, M. The optimized interface engineering of VS2 as cathodes for high performance all-solid-state lithium-ion battery. *Sci. China Technol. Sci.* **2022**, *65*, 1859–1866. [[CrossRef](#)]
6. Chong, P.; Zhou, Z.; Wang, K.; Zhai, W.; Li, Y.; Wang, J.; Wei, M. The Stabilizing of 1T-MoS2 for All-Solid-State Lithium-Ion Batteries. *Batteries* **2023**, *9*, 26. [[CrossRef](#)]
7. Yu, X.; Yao, Y.; Wang, X.; Cen, S.; Li, D.; Ma, H.; Chen, J.; Wang, D.; Mao, Z.; Dong, C. Rapid ultrasound welding toward compact Na/Beta- Al_2O_3 interface realizing room-temperature solid-state sodium metal battery. *Energy Storage Mater.* **2023**, *54*, 221–226. [[CrossRef](#)]
8. Lei, D.; He, Y.-B.; Huang, H.; Yuan, Y.; Zhong, G.; Zhao, Q.; Hao, X.; Zhang, D.; Lai, C.; Zhang, S.; et al. Cross-linked beta alumina nanowires with compact gel polymer electrolyte coating for ultra-stable sodium metal battery. *Nat. Commun.* **2019**, *10*, 4244. [[CrossRef](#)]
9. Liu, L.; Su, J.; Zhou, X.; Liang, D.; Liu, Y.; Tang, R.; Xu, Y.; Jiang, Y.; Wei, Z. Conductivity versus structure dependence investigation of $\text{Na}_{1+x}\text{Zr}_2\text{Si}_x\text{P}_{3-x}\text{O}_{12}$ ($0 \leq x \leq 3$) through composition optimization by adjusting Si/P ratio. *Mater. Today Chem.* **2023**, *30*, 101495. [[CrossRef](#)]
10. Park, H.; Jung, K.; Nezafati, M.; Kim, C.-S.; Kang, B. Sodium Ion Diffusion in Nasicon ($\text{Na}_3\text{Zr}_2\text{Si}_2\text{PO}_{12}$) Solid Electrolytes: Effects of Excess Sodium. *ACS Appl. Mater. Interfaces* **2016**, *8*, 27814–27824. [[CrossRef](#)] [[PubMed](#)]
11. Li, Y.; Deng, Z.; Peng, J.; Chen, E.; Yu, Y.; Li, X.; Luo, J.; Huang, Y.; Zhu, J.; Fang, C.; et al. A P2-Type Layered Superionic Conductor Ga-Doped $\text{Na}_2\text{Zn}_2\text{TeO}_6$ for All-Solid-State Sodium-Ion Batteries. *Chemistry* **2018**, *24*, 1057–1061. [[CrossRef](#)] [[PubMed](#)]

12. Li, Y.; Deng, Z.; Peng, J.; Gu, J.; Chen, E.; Yu, Y.; Wu, J.; Li, X.; Luo, J.; Huang, Y.; et al. New P2-Type Honeycomb-Layered Sodium-Ion Conductor: $\text{Na}_2\text{Mg}_2\text{TeO}_6$. *ACS Appl. Mater. Interfaces* **2018**, *10*, 15760–15766. [[CrossRef](#)] [[PubMed](#)]
13. Huang, H.; Yang, Y.; Chi, C.; Wu, H.-H.; Huang, B. Phase stability and fast ion transport in P2-type layered $\text{Na}_2\text{X}_2\text{TeO}_6$ (X = Mg, Zn) solid electrolytes for sodium batteries. *J. Mater. Chem. A* **2020**, *8*, 22816–22827. [[CrossRef](#)]
14. Dong, Y.F.; Wen, P.C.; Shi, H.D.; Yu, Y.; Wu, Z.S. Solid-State Electrolytes for Sodium Metal Batteries: Recent Status and Future Opportunities. *Adv. Funct. Mater.* **2023**, *21*, 2213584. [[CrossRef](#)]
15. Hayashi, A.; Masuzawa, N.; Yubuchi, S.; Tsuji, F.; Hotehama, C.; Sakuda, A.; Tatsumisago, M. A sodium-ion sulfide solid electrolyte with unprecedented conductivity at room temperature. *Nat. Commun.* **2019**, *10*, 5266. [[CrossRef](#)] [[PubMed](#)]
16. Li, F.; Hou, M.; Zhao, L.; Zhang, D.; Yang, B.; Liang, F. Electrolyte and interface engineering for solid-state sodium batteries. *Energy Storage Mater.* **2024**, *65*, 103181. [[CrossRef](#)]
17. Tachez, M.; Malugani, J.-P.; Mercier, R.; Robert, G. Ionic conductivity of and phase transition in lithium thiophosphate Li_3PS_4 . *Solid State Ionics* **1984**, *14*, 181–185. [[CrossRef](#)]
18. Jansen, M.; Henseler, U. Synthesis, Structure Determination, and Ionic-Conductivity of Sodium Tetrathiophosphate. *J. Solid State Chem.* **1992**, *99*, 110–119. [[CrossRef](#)]
19. Wu, E.A.; Kompella, C.S.; Zhu, Z.; Lee, J.Z.; Lee, S.C.; Chu, I.-H.; Nguyen, H.; Ong, S.P.; Banerjee, A.; Meng, Y.S. New Insights into the Interphase between the Na Metal Anode and Sulfide Solid-State Electrolytes: A Joint Experimental and Computational Study. *ACS Appl. Mater. Interfaces* **2018**, *10*, 10076–10086. [[CrossRef](#)]
20. Ma, Q.; Tietz, F. Solid-State Electrolyte Materials for Sodium Batteries: Towards Practical Applications. *ChemElectroChem* **2020**, *7*, 2693–2713. [[CrossRef](#)]
21. Li, Y.; Arnold, W.; Halacoglu, S.; Jasinski, J.B.; Druffel, T.; Wang, H. Phase-Transition Interlayer Enables High-Performance Solid-State Sodium Batteries with Sulfide Solid Electrolyte. *Adv. Funct. Mater.* **2021**, *31*, 2101636. [[CrossRef](#)]
22. Zhang, L.; Zhang, D.; Yang, K.; Yan, X.; Wang, L.; Mi, J.; Xu, B.; Li, Y. Vacancy-Contained Tetragonal Na_3SbS_4 Superionic Conductor. *Adv. Sci.* **2016**, *3*, 1600089. [[CrossRef](#)] [[PubMed](#)]
23. Feng, X.; Chien, P.-H.; Zhu, Z.; Chu, I.-H.; Wang, P.; Immediato-Scuotto, M.; Arabzadeh, H.; Ong, S.P.; Hu, Y.-Y. Studies of Functional Defects for Fast Na-Ion Conduction in $\text{Na}_{3-y}\text{PS}_{4-x}\text{Cl}_x$ with a Combined Experimental and Computational Approach. *Adv. Funct. Mater.* **2019**, *29*, 1807951. [[CrossRef](#)]
24. Tsuji, F.; Masuzawa, N.; Sakuda, A.; Tatsumisago, M.; Hayashi, A. Preparation and Characterization of Cation-Substituted Na_3SbS_4 Solid Electrolytes. *ACS Appl. Energy Mater.* **2020**, *3*, 11706–11712. [[CrossRef](#)]
25. Yu, L.; Jiao, Q.; Liang, B.; Shan, H.; Lin, C.; Gao, C.; Shen, X.; Dai, S. Exceptionally high sodium ion conductivity and enhanced air stability in Na_3SbS_4 via germanium doping. *J. Alloys Compd.* **2022**, *913*, 165229. [[CrossRef](#)]
26. Jalem, R.; Gao, B.; Tian, H.-K.; Tateyama, Y. Theoretical study on stability and ion transport property with halide doping of Na_3SbS_4 electrolyte for all-solid-state batteries. *J. Mater. Chem. A* **2022**, *10*, 2235–2248. [[CrossRef](#)]
27. Yu, L.; Yin, J.; Gao, C.; Lin, C.; Shen, X.; Dai, S.; Jiao, Q. Halogen Doping Mechanism and Interface Strengthening in the Na_3SbS_4 Electrolyte via Solid-State Synthesis. *ACS Appl. Mater. Interfaces* **2023**, *15*, 31635–31642. [[CrossRef](#)] [[PubMed](#)]
28. Fu, Y.; Gong, Z.; Li, D.; Liu, Y.; Zhou, X.; Yang, Y.; Jiao, Q. Zn doping for enhanced sodium-ion conductivity and air stability in Na_3SbS_4 solid electrolyte. *J. Mater. Sci.* **2024**, *59*, 3009–3017. [[CrossRef](#)]
29. Kamaya, N.; Homma, K.; Yamakawa, Y.; Hirayama, M.; Kanno, R.; Yonemura, M.; Kamiyama, T.; Kato, Y.; Hama, S.; Kawamoto, K.; et al. A lithium superionic conductor. *Nat. Mater.* **2011**, *10*, 682–686. [[CrossRef](#)] [[PubMed](#)]
30. Weber, D.A.; Senyshyn, A.; Weldert, K.S.; Wenzel, S.; Zhang, W.; Kaiser, R.; Berendts, S.; Janek, J.; Zeier, W.G. Structural Insights and 3D Diffusion Pathways within the Lithium Superionic Conductor $\text{Li}_{10}\text{GeP}_2\text{S}_{12}$. *Chem. Mater.* **2016**, *28*, 5905–5915. [[CrossRef](#)]
31. Dawson, J.A.; Islam, M.S. A Nanoscale Design Approach for Enhancing the Li-Ion Conductivity of the $\text{Li}_{10}\text{GeP}_2\text{S}_{12}$ Solid Electrolyte. *ACS Mater. Lett.* **2022**, *4*, 424–431. [[CrossRef](#)] [[PubMed](#)]
32. Kato, Y.; Hori, S.; Kanno, R. $\text{Li}_{10}\text{GeP}_2\text{S}_{12}$ -Type Superionic Conductors: Synthesis, Structure, and Ionic Transportation. *Adv. Energy Mater.* **2020**, *10*, 2002153. [[CrossRef](#)]
33. Richards, W.D.; Tsujimura, T.; Miara, L.J.; Wang, Y.; Kim, J.C.; Ong, S.P.; Uechi, I.; Suzuki, N.; Ceder, G. Design and synthesis of the superionic conductor $\text{Na}_{10}\text{SnP}_2\text{S}_{12}$. *Nat. Commun.* **2016**, *7*, 11009. [[CrossRef](#)] [[PubMed](#)]
34. Zhang, Z.; Ramos, E.; Lalère, F.; Assoud, A.; Kaup, K.; Hartman, P.; Nazar, L.F. $\text{Na}_{11}\text{Sn}_2\text{PS}_{12}$: A new solid state sodium superionic conductor. *Energy Environ. Sci.* **2018**, *11*, 87–93. [[CrossRef](#)]
35. Duchardt, M.; Ruschewitz, U.; Adams, S.; Dehnen, S.; Røling, B. Vacancy-Controlled Na^+ Superion Conduction in $\text{Na}_{11}\text{Sn}_2\text{PS}_{12}$. *Angew. Chem. Int. Ed.* **2018**, *57*, 1351–1355. [[CrossRef](#)] [[PubMed](#)]
36. Kandagal, V.S.; Bharadwaj, M.D.; Waghmare, U.V. Theoretical prediction of a highly conducting solid electrolyte for sodium batteries: $\text{Na}_{10}\text{GeP}_2\text{S}_{12}$. *J. Mater. Chem. A* **2015**, *3*, 12992–12999. [[CrossRef](#)]
37. Nunotani, N.; Ohsaka, T.; Tamura, S.; Imanaka, N. Tetravalent Sn^{4+} Ion Conductor Based on NASICON-Type Phosphate. *ECS Electrochem. Lett.* **2012**, *1*, A66. [[CrossRef](#)]
38. Boulineau, S.; Courty, M.; Tarascon, J.-M.; Viallet, V. Mechanochemical synthesis of Li-argyrodite $\text{Li}_6\text{PS}_5\text{X}$ (X=Cl, Br, I) as sulfur-based solid electrolytes for all solid state batteries application. *Solid State Ionics* **2012**, *221*, 1–5. [[CrossRef](#)]
39. Deiseroth, H.J.; Kong, S.T.; Eckert, H.; Vannahme, J.; Reiner, C.; Zaiss, T.; Schlosser, M. $\text{Li}_6\text{PS}_5\text{X}$: A class of crystalline Li-rich solids with an unusually high Li^+ mobility. *Angew. Chem. Int. Ed.* **2008**, *47*, 755–758. [[CrossRef](#)] [[PubMed](#)]

40. Studenyak, I.P.; Pogodin, A.I.; Studenyak, V.I.; Kokhan, O.P.; Azhniuk, Y.M.; Solonenko, D.; Daróczy, L.; Kökényesi, S.; Zahn, D.R.T. Structural, electrical and optical properties of ion-conducting $\text{Na}_6\text{PS}_5\text{Cl}$, $\text{Na}_6\text{PS}_5\text{Br}$, and Na_7PS_6 compounds. *J. Phys. Chem. Solids* **2021**, *159*, 110269. [[CrossRef](#)]
41. Adeli, P.; Bazak, J.D.; Park, K.H.; Kochetkov, I.; Huq, A.; Goward, G.R.; Nazar, L.F. Boosting Solid-State Diffusivity and Conductivity in Lithium Superionic Argyrodites by Halide Substitution. *Angew. Chem. Int. Ed.* **2019**, *58*, 8681–8686. [[CrossRef](#)] [[PubMed](#)]
42. Stamminger, A.R.; Ziebarth, B.; Mrovec, M.; Hammerschmidt, T.; Drautz, R. Ionic Conductivity and Its Dependence on Structural Disorder in Halogenated Argyrodites $\text{Li}_6\text{PS}_5\text{X}$ ($\text{X} = \text{Br}, \text{Cl}, \text{I}$). *Chem. Mater.* **2019**, *31*, 8673–8678. [[CrossRef](#)]
43. Gao, L.; Xie, Y.; Tong, Y.; Xu, M.; You, J.; Wei, H.; Yu, X.; Xu, S.; Zhang, Y.; Che, Y.; et al. Lithium-site substituted argyrodite-type $\text{Li}_6\text{PS}_5\text{I}$ solid electrolytes with enhanced ionic conduction for all-solid-state batteries. *Sci. China Technol. Sci.* **2023**, *66*, 2059–2068. [[CrossRef](#)]
44. Haznar, A.; Pietraszko, A.; Studenyak, I.P. X-ray study of the superionic phase transition in $\text{Cu}_6\text{PS}_5\text{Br}$. *Solid State Ionics* **1999**, *119*, 31–36. [[CrossRef](#)]
45. Nilges, T.; Pfitzner, A. A structural differentiation of quaternary copper argyrodites: Structure—Property relations of high temperature ion conductors. *Z. Kristallogr. Cryst. Mater.* **2005**, *220*, 281–294. [[CrossRef](#)]
46. Momma, K.; Izumi, F. VESTA 3 for three-dimensional visualization of crystal, volumetric and morphology data. *J. Appl. Crystallogr.* **2011**, *44*, 1272–1276. [[CrossRef](#)]
47. Zhao, G.; Suzuki, K.; Hirayama, M.; Kanno, R. Syntheses and Characterization of Novel Perovskite-Type LaScO_3 -Based Lithium Ionic Conductors. *Molecules* **2021**, *26*, 299. [[CrossRef](#)] [[PubMed](#)]
48. Zhao, G.; Suzuki, K.; Hirayama, M.; Kanno, R. Synthesis and Lithium-ion Conductivity of $\text{Sr}(\text{La}_{1-x}\text{Li}_3\text{x})\text{ScO}_4$ with a K_2NiF_4 Structure. *Electrochemistry* **2022**, *90*, 017005. [[CrossRef](#)]
49. Zhao, G.; Suzuki, K.; Seki, T.; Sun, X.; Hirayama, M.; Kanno, R. High lithium ionic conductivity of γ - Li_3PO_4 -type solid electrolytes in Li_4GeO_4 - Li_4SiO_4 - Li_3VO_4 quasi-ternary system. *J. Solid State Chem.* **2020**, *292*, 121651. [[CrossRef](#)]
50. Jian, Z.; Sun, Y.; Ji, X. A new low-voltage plateau of $\text{Na}_3\text{V}_2(\text{PO}_4)_3$ as an anode for Na-ion batteries. *Chem. Commun.* **2015**, *51*, 6381–6383. [[CrossRef](#)] [[PubMed](#)]
51. Chu, I.-H.; Kompella, C.S.; Nguyen, H.; Zhu, Z.; Hy, S.; Deng, Z.; Meng, Y.S.; Ong, S.P. Room-Temperature All-solid-state Rechargeable Sodium-ion Batteries with a Cl-doped Na_3PS_4 Superionic Conductor. *Sci. Rep.* **2016**, *6*, 33733. [[CrossRef](#)] [[PubMed](#)]
52. Wan, H.; Mwizerwa, J.P.; Qi, X.; Xu, X.; Li, H.; Zhang, Q.; Cai, L.; Hu, Y.-S.; Yao, X. Nanoscaled Na_3PS_4 Solid Electrolyte for All-Solid-State FeS_2/Na Batteries with Ultrahigh Initial Coulombic Efficiency of 95% and Excellent Cyclic Performances. *ACS Appl. Mater. Interfaces* **2018**, *10*, 12300–12304. [[CrossRef](#)] [[PubMed](#)]
53. Nguyen, H.; Banerjee, A.; Wang, X.; Tan, D.; Wu, E.A.; Doux, J.-M.; Stephens, R.; Verbist, G.; Meng, Y.S. Single-step synthesis of highly conductive Na_3PS_4 solid electrolyte for sodium all solid-state batteries. *J. Power Sources* **2019**, *435*, 126623. [[CrossRef](#)]

Disclaimer/Publisher’s Note: The statements, opinions and data contained in all publications are solely those of the individual author(s) and contributor(s) and not of MDPI and/or the editor(s). MDPI and/or the editor(s) disclaim responsibility for any injury to people or property resulting from any ideas, methods, instructions or products referred to in the content.